Journal Pre-proof

Fatigue life prediction of a L-PBF component in Ti-6Al-4V using sample data, FE-based simulations and machine learning

Antonio Cutolo, Nicolas Lammens, Koen Vanden Boer, Hunor Erdelyi, Matthias Schulz, Gokula Krishna Muralidharan, Lore Thijs, Chola Elangeswaran, Brecht Van Hooreweder

PII: S0142-1123(22)00526-6
DOI: https://doi.org/10.1016/j.ijfatigue.2022.107276
Reference: JIJF 107276

To appear in: *International Journal of Fatigue*

Received date : 13 May 2022
Revised date : 6 September 2022
Accepted date : 14 September 2022

Please cite this article as: A. Cutolo, N. Lammens, K.V. Boer et al., Fatigue life prediction of a L-PBF component in Ti-6Al-4V using sample data, FE-based simulations and machine learning. *International Journal of Fatigue* (2022), doi: https://doi.org/10.1016/j.ijfatigue.2022.107276.

Fatigue life prediction of a L-PBF component in Ti-6Al-4V using sample data, FE-based simulations and machine learning

Antonio Cutolo[a,b], Nicolas Lammens[c], Koen Vanden Boer[d], Hunor Erdelyi[c], Matthias Schulz[f], Gokula Krishna Muralidharan[e], Lore Thijs[e], Chola Elangeswaran[a,b], Brecht Van Hooreweder[a,1]

[a]*KU Leuven Department of Mechanical Engineering, Celestijnenlaan 300, 3001 Leuven (Heverlee), Belgium*
[b]*SIM M3 Program, Technologiepark 48, 9052 Zwijnaarde, Belgium*
[c]*Siemens Digital Industries Software, Interleuvenlaan 68, 3001 Leuven, Belgium*
[d]*Flanders Make, Oude Diestersebaan 133, 3920 Lommel, Belgium*
[e]*3D Systems Leuven, Grauwmeer 14, 3001, Leuven, Belgium*
[f]*Siemens Industry Software GmbH, Luxemburger Str. 7, Kaiserslautern, Germany*

Abstract

Laser Powder Bed Fusion (L-PBF) is a widely-used additive manufacturing (AM) technique for producing complex metal parts used for a variety of dynamically loaded applications. Fatigue performance of standardized L-PBF samples is at present fairly well understood, while the knowledge on the fatigue behaviour of real-life complex shaped components is often lacking. This work presents insight, methods and results on predicting L-PBF component fatigue life using FE-based simulations, stress-based sample fatigue data and machine learning respectively. A realistic end-use part with representative geometry for many industrial applications was selected and produced in Ti-6Al-4V by L-PBF along with many standardized samples under different building orientations and with different types of heat treatments and surface finishing steps. The results indicate that the developed tool for component fatigue life prediction can accurately predict both the failure location and the number of cycles to failure.

Keywords: laser powder bed fusion - Ti-6Al-4V - fatigue life - machine-learning

Introduction

Additive Manufacturing (AM) is increasingly being used as a production technique for functional parts in a variety of applications. Laser Powder Bed Fusion (L-PBF), also known as Selective Laser Melting (SLM), is a widely used AM technique for processing a variety of metals to form complex three-dimensional parts.

L-PBF has been successfully used in the last three decades to produce parts in a variety of metals, from which 316L, Ti-6Al-4V and AlSi10Mg are amongst the most widely used and reported [1, 2, 3, 4]. From these materials, Ti-6Al-4V is frequently used for applications that need light weight, good biocompatibility and/or good corrosion resistance and/or high performance under increased thermal and/or mechanical loads. In most of these applications, also the fatigue performance of the material is important. The fatigue behaviour of titanium alloys produced by LPBF has hence been studied intensively during the past ten years.

Multiple studies have analysed the influence of heat treatments, surface treatments and build orientation on different aspects of fatigue behaviour. In as-built state, Ti-6Al-4V produced by L-PBF is usually characterised by a fine acicular α' martensitic microstructure. Compared to a coarser mill annealed microstructure, Van Hooreweder et al. [5] showed that L-PBF Ti-6Al-4V exhibits reduced fracture toughness due to this unstable martensitic matrix. Heat treatment operations lead to a transformation of the martensite into various forms of $\alpha + \beta$ microstructure [6]. An increase in ductility is reported after such transformation. Therefore, owing to the ease of slip transfer across the

*Corresponding author
Email address: brecht.vanhooreweder@kuleuven.be (Brecht Van Hooreweder)
URL: www.set.kuleuven.be/am/ (Brecht Van Hooreweder)

α/β interface, a higher fatigue performance is generally observed. A number of studies report the fatigue results of L-PBF Ti-6Al-4V after stress relief, annealing and HIP treatments. From the analysis of data reported in literature, despite the effect of the different microstructure on Ti-6Al-4V fatigue performance [7], it has been observed that the most dominant influencing factors were found to be surface conditions, porosity and defects. Lack of fusion voids, gas pores, un-molten particles and small cracks can indeed act as fatigue crack initiation sites. Combined with such defects, the rough surface obtained after L-PBF induces micro-notch like effects that further accelerate the crack initiation behaviour. Günther et al. [8] verified this concept by testing machined fatigue samples with internal channels. They observed that cracks initiated from the as-fabricated surface of internal channels. Samples with reduced channel diameters exhibited higher fatigue lives. Surface treatment operations such as machining remove the stress concentration effects and enhance the fatigue performance [9]. Fatemi et al. [10] performed multiaxial fatigue tests and found that the results remained similar to those of torsional tests; i.e., the fatigue performance of machined samples was better than the fatigue performance of non-machined samples. However, one of the main advantages of AM techniques over the conventional manufacturing methods is the ability to produce parts with complex geometries as net shape, and therefore the machining operations of such intricate geometries might be difficult if not impossible in some cases [11].

Another important aspect that significantly impacts the AM Ti-6Al-4V fatigue performance can be associated to the part orientation with respect to the building direction. In fact, inclined surfaces might present poorer surface quality with respect to the vertical surfaces as they are affected by the staircase effect on up-facing surfaces and dross formation on down-facing surfaces. These two phenomena have been considered as detrimental factors for fatigue performance of AM Ti-6Al-4V samples in as-produced surface condition [12].

Besides the effect of the surface conditions, recent reviews on fatigue performance of AM Ti-6Al-4V samples [11, 13] also summarized how volume post-treatments influence the material fatigue properties. In particular Singla et al. [13] highlighted how HIP has been considered by several authors [11, 14, 15] as a powerful post-treatment to minimize the defect population and size with a consequent beneficial impact on fatigue performance. However, the enhancement of AM Ti-6Al-4V fatigue properties consequent to a HIP post-process can only be appreciated on machined coupons. In fact Cutolo et al. [16] concluded that for specimens with an as-produced surface, the HIP treatment was not able to improve the L-PBF Ti-6Al-4V fatigue behaviour as does a straightforward and economically competitive stress relieving treatment. The reason for that was attributed to the difference in microstructure generated by stress relieving (SR) and HIP. In particular the fine $\alpha + \beta$ microstructure generated by SR guaranteed a higher resistance to crack initiation with respect to the coarse $\alpha + \beta$ microstructure generated by HIP.

The large majority of scientific articles dealing with fatigue of LPBF produced titanium focuses on investigations at the sample scale with test geometries ranging from classical cuboids to standardized tensile and fatigue test samples. These geometries are significantly different from the complex three-dimensional geometries that are eventually used in real-life applications. Using sample (fatigue) data to predict the mechanical behaviour and fatigue life of a LPBF component in Ti-6Al-4V is, however, not a straightforward task. Indeed, many local factors such as surface roughness, microstructure, loading and stresses, defects, etc. should be accurately accounted for [17].

According to the knowledge of the authors, this paper is among the first studies that present and discuss validated approaches for fatigue life prediction of L-PBF produced components in Ti-6Al-4V. The presented tools, methodology and insights can also be extended towards other AM technologies and materials. Recently Molaei et al. [18] and Li et al. [19] predicted the fatigue behaviour of a Ti-6Al-4V aerospace component. Extreme value statistics of defects was used to calculate the effective defect size for fatigue life predictions. Although the predicted stress concentration zone coincided with the experimental crack initiation site, the hotspot surface was machined. As a result, no L-PBF-related surface influential factors were considered.

This paper extends upon the fatigue life prediction methods for complex geometries produced by AM as presented by Elangeswaran et al. [20]. The tools and approaches presented by the aforementioned study by Elangeswaran et al. are extended and used for the fatigue life prediction of an industrially relevant benchmark part in Ti-6Al-4V.

First of all, in order to build a L-PBF Ti-6Al-4V fatigue database, an extensive experimental campaign was performed on coupon level, considering different combinations of building orientations, volume and surface treatments. Using machine learning and physical understanding of the material, a simulation-based fatigue life prediction of an industrial Ti-6Al-4V demonstrator produced by L-PBF was then performed. This demonstrator presents many of the typical features of additively manufactured components such as thin walls, overhanging surfaces, and internal holes. The prediction was followed by an experimental validation of the fatigue life and failure location of the demonstrator.

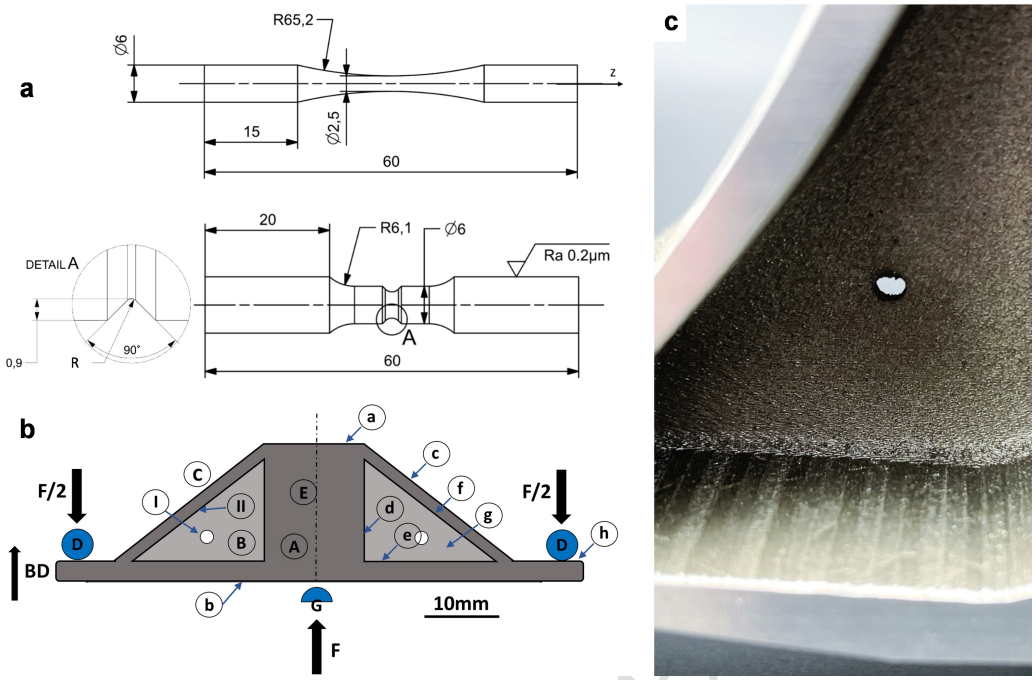

Figure 1: (a) Fatigue sample geometries produced by L-PBF in Ti-6Al-4V (dimensions in mm): plain and notched specimen geometries. For notched coupons, three different radii have been considered. (b) Industrial demonstrator geometry produced by L-PBF in Ti-6Al-4V, with indication of the fatigue loading, build direction (BD), bulky zone (A), internal flange (B), thin features (C), support rollers (D), symmetry line (E), loads (F), connection with the actuator (G) and critical zones for fatigue crack initiation (I) and (II), and from *a* to *h* the roughness measurement regions. (c) internal flange including the hole of the produced L-PBF part.

Finally, a comparison between the predicted lifetime and the experimental fatigue life was performed. The results indicate that the crack initiation point in the industrial benchmark part can be accurately predicted. In addition, the predicted number of load cycles leading to crack initiation in the life range of 10^4 to 10^6 cycles for three different loading conditions corresponds well with the actual fatigue life in the same life range.

Materials and methods

Samples and component design

Figure 1-(a) shows the miniature fatigue sample design used in this work with continuously reducing fillet and critical cross-section of diameter 2.5*mm*. Fatigue behaviour of this geometry was validated in previous studies [16, 21, 22, 23]. The miniature fatigue samples were printed under various build directions (BD). BD was defined as the angle between the specimen z axis (Figure 1-(a)) and the build platform of the L-PBF system. Furthermore, Figure 1-(a) shows the notched specimen geometry.

The geometry of the industrial demonstrator is indicated in Figure 1-(b). The industrial demonstrator was produced under a fixed build direction as indicated in Figure 1-(b). The design of the demonstrator was conceived to include in one geometry the typical critical features of additively manufactured parts, such as thin walls represented by region **B** of Figure 1-(b), overhanging surfaces (feature II of Figure 1-(b)), passing holes (feature I of Figure 1-(b)). The passing holes have not been machined, since they were intended to replicate powder removal hole.

Material and manufacturing

All samples and components used in this study were produced using a commercial DMP ProX320 LPBF machine (3DSystems-LayerWise, Leuven, Belgium) equipped with a 500W fiber laser and with vacuum chamber technology to reduce oxygen levels during production to below 50*ppm*. Gas atomized LaserForm® Ti-6Al-4V powder was

used. A layer thickness of 60μm was used with the L-PBF parameters corresponding to officially released LaserForm Ti-6Al-4V standard [24].

Two different volumetric thermal treatments were performed on L-PBF Ti-6Al-4V samples: stress relief (SR) and hot isostatic pressing (HIP). The stress relieving operation consists of heating the samples at a temperature of 850°C for 2h followed by air cooling. The HIP operation was performed at 920°C with a pressure of 100MPa for 2h, followed by furnace cooling.

Ti-6Al-4V samples underwent two different surface treatments: electro-plasma polishing (EPP) and machining (MC). EPP was performed by Plasmatec B.V. by submerging the samples in a plasma cloud, using their default parameters for titanium. After this operation, a 130μm reduction in diameter was observed and accounted for. The machined samples were turned down from oversized hexagonal bars to the final geometry, aiming at a surface roughness smaller than 0.2μm R_a. For each investigated condition three building orientations with respect to the baseplate were considered, i.e. vertical (90°), horizontal (0°) and inclined (50°). A summary of all the conditions investigated is presented in Table 1.

Table 1: Different process conditions employed for fatigue analysis.

Build orientation	Material condition	Surface condition
Vertical (90°)	As-built (AB)	Non-machined (NM)
Horizontal (0°)	Stress-relieved (SR)	Electro plasmapolished (EPP)
Inclined (50°)	HIP	Machined (MC)

The notched specimens were obtained from hexagonal bars that underwent SR operation and that were subsequently machined to the final geometry of Figure 1-(a). Three different radii R have been considered, i.e. 1.5, 0.50, and 0.25mm, corresponding to stress concentration factors k_t equals to 1.58, 2.25 and 3.09 respectively. Notched coupons have been produced under a fixed BD, i.e. z axis perpendicular to the build plate.

The industrial component was produced with layers perpendicular to the building direction (BD) indicated in Figure 1-(b). One volumetric post-treatment was performed after production on the industrial component, namely a stress relieving operation consisting of heating the components at a temperature of 850° C for 2h followed by air cooling. Except for zones *a* and *b* indicated in Figure 1-(b), the external surfaces were considered in their as-produced state. Zones *a* and *b* were, instead, machined to remove the as as-produced roughness. This machining operation is done for facilitating the fatigue testing only, as zones *a* and *b* will indeed not be the critical zones for fatigue failure.

Fatigue life prediction

Fatigue life prediction was achieved using FE analysis in Siemens Simcenter 3D to derive the stress fields under the defined loading conditions, and subsequent durability analysis using a custom developed code in the Open Solver interface of the Siemens Simcenter 3D Specialist Durability solver.

The FE analysis was performed on a one-quarter model of the actual geometry, exploiting symmetries in the geometry and the loading conditions. The boundary conditions were modelled as a rigid cylinder (D in Figure 1-(b)) at the bottom of the component with a frictionless contact defined between specimen and cylinder. The force was introduced at the top of the model and distributed over the contact area between the load-application fixture and the specimen. Quadratic CTETRA(10) elements were used in the model, with an average element size of 1mm throughout the component. Mesh refinements down to 0.1mm element size were applied in regions of high stress, resulting in a total mesh size of approximately 400,000 elements. A linear-elastic material definition corresponding to the measured static properties of Ti-6Al-4V was used, as well as a static, linear (SOL101) analysis method using the NX Nastran FE solver. Global convergence of the models was checked by comparing the force-displacement behaviour of the FE- model vs. static loading experiments performed on the component. Agreement down to the resolution of the employed sensors was achieved.

STL scans from actually printed components were converted into FE models with model parameters similar to the procedure described above (based on the CAD model). While small differences could be observed between actual and theoretical components, the critical regions in the model (zones I and II in Figure 1-(b)) were not affected by the impact of geometric tolerances. As such, all further analyses were performed on the CAD-based FE analysis.

Subsequent to the FE static analysis, durability calculations were performed using the Open Solver interface of the Siemens Simcenter 3D Specialist Durability software. A custom computation was implemented based on a Machine Learning approach, in order to account for the localized material features within the AM component. For more information, the reader is referred to Elangeswaran et al. [20] where the process is described for stainless steel 316L. A similar approach, with modified covariance and mean function definitions was applied to model the Ti-6Al-4V material under influence of the parameters listed in Table 1. The fatigue prediction methodology is represented in Figure 2.

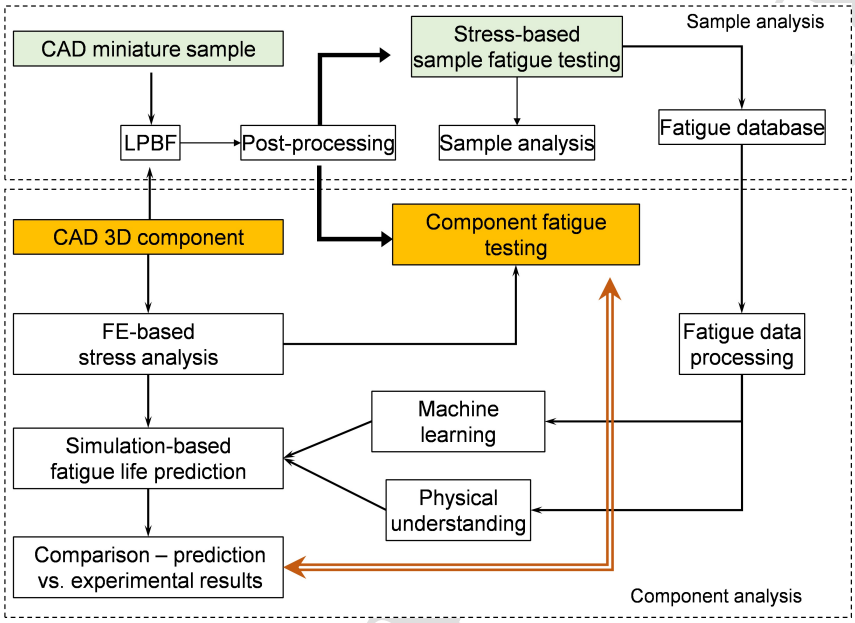

Figure 2: Schematic illustrating the work-flow for simulation-based fatigue life prediction of metal L-PBF components (adapted from [20]).

The upper block of the schematic involves the analysis of material fatigue performance on sample level that culminates in the definition of a stress-based fatigue database that accounts for the different fatigue influencing factors, i.e. surface and volume treatments, building orientations, mean-stress dependency, and notch factors. The lower block involves the fatigue analysis of the demonstrator. The stress-based fatigue data are processed and machine learning tools as well as empirical laws are developed to relate the influencing factors with the component fatigue life.

The life prediction approach is a modified stress life approach. In the first phase of the analysis, the complex (and/or multi-axial) load history is reduced into its fundamental load cycles. Each fundamental load cycle is characterized by its stress amplitude and mean stress (derived from the combination of the FE stress analysis and the load history), as well as the number of repetitions in the full load history. Common rain-flow counting methods are often used, while the Siemens Simcenter 3D Specialist Durability solver relies on the so-called hysteresis operator to achieve this step. For the present case of simple, constant-amplitude loads, the entire load history is essentially reduced to a single cycle.

Each fundamental load cycle is then further processed to compensate for mean stress effects. For this study, the Walker equation was used, as reported by Cutolo et al. [25]. After mean stress compensation, each fundamental load cycle is characterized by only its equivalent stress amplitude (in absence of mean stress) and the repetitions in the load history.

The final step in the stress life approach is to convert stress in each element (for each fundamental stress cycle) into an equivalent lifetime and damage value. In the present work, conventional S-N curves have been replaced by a machine learning methodology. In contrast to a single (or few) pre-determined S-N curve, the machine learning approach allows for prediction lifetime for each element considering its unique set of features (surface roughness, the angle between principal stress direction and print direction, global heat treatments, etc.). Essentially, through the

machine learning algorithm, each individual element gets assigned a unique S-N curve tuned to the local conditions present at that element.

The full load history is repeated and damages for each fundamental cycle are summed until a critical damage value (usually close to 1) is reached within the model, leading to the final prediction of a component lifetime. During the learning phase of machine learning, only coupon test data is used. The full set of coupon test results is split, where a part is used for training, and the remainder is used for validation (this has been repeated several times for different divisions of the full set of test data, to quantify the robustness of the hyperparameters). For the component lifetime assessment, none of the experimental results on the component were used as training for machine learning.

The outcome of the Durability analysis provides an element-by-element prediction of fatigue life. External post-processing was performed to compensate for notch effects near the surface of critical area I before comparing numerical predictions to experimental results.

Motivation for using supervised machine learning

Different process parameters, post-production procedures, and physical characteristics can yield different material fatigue performance for L-PBF parts. Even though an extensive test campaign was conducted, it was not yet able to obtain a parametric description of how the various fatigue-influencing factors interacted. This demands for the selection of a non-parametric probabilistic model along with a model parameter identification. In this article, a Gaussian process regression, a supervised machine learning algorithm, is used as proposed by Elangeswaran et al.[20]. A Gaussian process is considered supervised a machine learning approach since the modeller must select a covariance function that describes the correlations between the input parameters (for more information, please refer to Appendix I). By using such a process, it is possible to eliminate the issue of finding a parametric description of the problem. A multidimensional vector with known data regarding process parameters, surface and material state, and physical attributes is used as input by the Gaussian process to forecast fatigue performance. The mean and standard deviation of the material fatigue life are the procedure' outputs.

Fatigue testing

Coupon testing

Axial tension-compression fatigue tests were performed on the miniaturised samples at zero mean stress. An Instron E10000 fatigue set-up with a $10kN$ load cell and pneumatic grips was used for the tests. Load-controlled sinusoidal constant amplitude stresses were applied at a frequency of $30Hz$. For each stress amplitude (σ_a), the number of cycles to failure, stiffness degradation of 5% or run-out at $2 \cdot 10^6$ cycles was noted as N_f, whichever is the earliest occurrence. The observed data points were fitted with Basquin's equation ($\sigma_a = A(2N_f)^b$), where A and b are material constants , to obtain a stress-life (SN) plot.

Fatigue tests were conducted with a stress-ratio $R = -1$. For stress-relieved coupons, produced vertically, stress-ratio $R = 0.1$ and $R = 0.5$ were also investigated.

In order to evaluate the fatigue strength of the material, the step procedure illustrated by Nicholas et al. [26] and validated by Bellows et al. [27] was used. In particular, the fatigue strength at $2 \cdot 10^6$ cycles was calculated via the following equation:

$$\sigma_{a_{2\cdot10^6}} = \sigma_{N-1} + \Delta\sigma\left(\frac{N_f}{2 \cdot 10^6}\right) \tag{1}$$

in which N_f is the number of cycles to failure, $\Delta\sigma$ is the stress step increment, σ_{N-1} is the previous stress amplitude that did not cause failure of the coupons.

Component testing

Fatigue tests were performed on the components with a load-ratio $R = 0.1$. The components were clamped in an actuator with a maximum load capacity of $25kN$. In order to reduce boundary conditions uncertainties, the component was simply supported on hardened cylinders on both sides (Figure 1-(b), part D). In this way the contact of the sample was reduced to a well-defined line contact, which could be accurately translated in the simulation. The force was transferred from the actuator to the component via a semi-cylindrical hardened bar and, in order to avoid misalignment effects, a flexible connection between the bar and the actuator was used to assure a uniform load distribution between the two sides of the component. Three different maximum load levels were investigated, i.e. 10.8, 12 and 14kN with a

frequency of 15Hz. 10 samples were tested in total. During each fatigue test, force and displacement were constantly monitored.

Sample and component analysis

For microstructural analysis, representative ground and polished samples were etched with modified Keller's reagent (95 mL H_20, 2.5 mL HNO_3, 1 mL HCl, 1.5 mL HF). Optical and scanning electron microscopy analysis were performed using Keyence VHX 6000 and Philips XL30 FEG systems, respectively. Archimedes method was used to determine the relative density of the samples. Besides, porosity was also observed with optical microscopy. Surface roughness was measured with a Mitutoyo Formtracer CS-3200S4 device. Three measurements were performed on each sample with an approximate rotation interval of 120°. Tensile tests were conducted on a Shimadzu AG-X Plus machine according to ASTM E8 specification, using a video extensometer for strain measurements. Post-fatigue fracture surfaces were analysed by SEM with Philips XL30 FEG.

Results and discussion

Microstructure, quasi-static properties and roughness measurements of samples

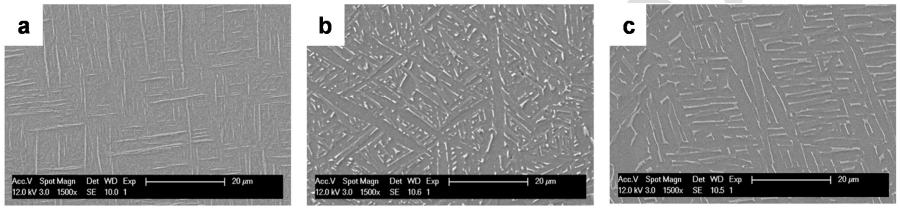

Figure 3: SEM images of as-built microstructure (a), stress relieved microstructure (b), and of HIP'ed microstructure (c)

Microstructures of the three material conditions are shown in Figure 3. A fine martensitic α' microstructure is obtained after L-PBF. SEM images represent this fine needle-like microstructure in Figure 3-(a), respectively. High cooling rates in L-PBF results in this metastable structure of α' phase supersaturated with β stabilising elements. This martensitic microstructure is transformed into a Widmanstätten or basketweave α+β microstructure after the stress relief heat treatment, as seen in Figure 3-(b). Precipitation of incoherent β particles at prior β phase boundaries or high dislocation density regions results in the decomposition of the α' phase into a dual phase α+β. A coarser α+β microstructure is obtained after HIP treatment as shown in Figure 3-(c). Temperatures higher than those in the stress relief treatment have evidently resulted in microstructure coarsening.

The tensile test results corresponding to as produced samples showed a yield stress $\sigma_y = 1086 \pm 15$ $[MPa]$, an ultimate tensile stress $\sigma_{UTS} = 1246 \pm 22$ $[MPa]$, and an elongation at fracture of 11 ± 1 $[\%]$. After volumetric post-treatments, stress relieved samples presented the following static properties $\sigma_y = 914 \pm 45$ $[MPa]$, $\sigma_{UTS} = 1002 \pm 30$ $[MPa]$, and an elongation at fracture of 16±3 [%], whereas for the HIP coupons $\sigma_y = 860 \pm 40$ $[MPa]$, $\sigma_{UTS} = 960 \pm 30$ $[MPa]$, and an elongation at fracture of 18 ± 4 $[\%]$ were measured.

Higher strength and limited elongation to fracture is observed in as-built condition, corresponding to the martensitic microstructure. Stress relief heat treatment has resulted in a drop in strength with increase in elongation to fracture, as expected from a dual phase α+β microstructure. The evidence of further microstructure coarsening through HIP is reflected in the additional decrease in strength and increase in elongation to fracture.

The roughness measurements performed on the sample coupons for all the conditions listed in Table 1 are reported in Table 2. The results indicate how electro-plasma polishing and machining operations can improve the surface quality of the LPBF Ti-6Al-4V samples significantly.

The EPP treatment was able to improve the surface quality of samples that were built vertically and with 50° orientation with respect to the baseplate. On the other hand, a small difference was measured for horizontally produced EPP samples with respect to non-machined ones. Given the geometry of the coupons, the reason for that could be attributed to the fact that for this particular orientation (i.e. 0°) the surface morphology is mainly influenced by a severe staircase effect and the EPP treatment was not able to smoothen this.

Table 2: Surface roughness summary for LPBF Ti-6Al-4V samples in all the different surface conditions and building orientations expressed in terms of mean values of R_a and R_v.

Surface condition	Building orientation	$R_a[\mu m]$	$R_v[\mu m]$
NM	0°	97.91	172.10
	50°	23.51	52.03
	90°	9.11	24.54
EPP	0°	33.11	110.70
	50°	7.09	25.32
	90°	2.67	9.11
MC	0° 50° 90°	0.11	0.4

Component surface roughness

One of the produced components was cut with EDM to evaluate the surface morphology and roughness around the critical locations. The measurements were performed at the locations indicated in Figure 1-(b) and the results are reported in Table 3.

Table 3: Surface roughness summary measured on the component critical regions indicated in Figure 1-(b).

Position	a	b	c	d	e	f	g	h
$R_a[\mu m]$	0.22	0.21	20.20	8.67	32.70	20.42	8.67	35.94
$R_v[\mu m]$	0.78	0.76	60.72	29.12	89.46	41.37	29.12	102.73

Sample fatigue behaviour

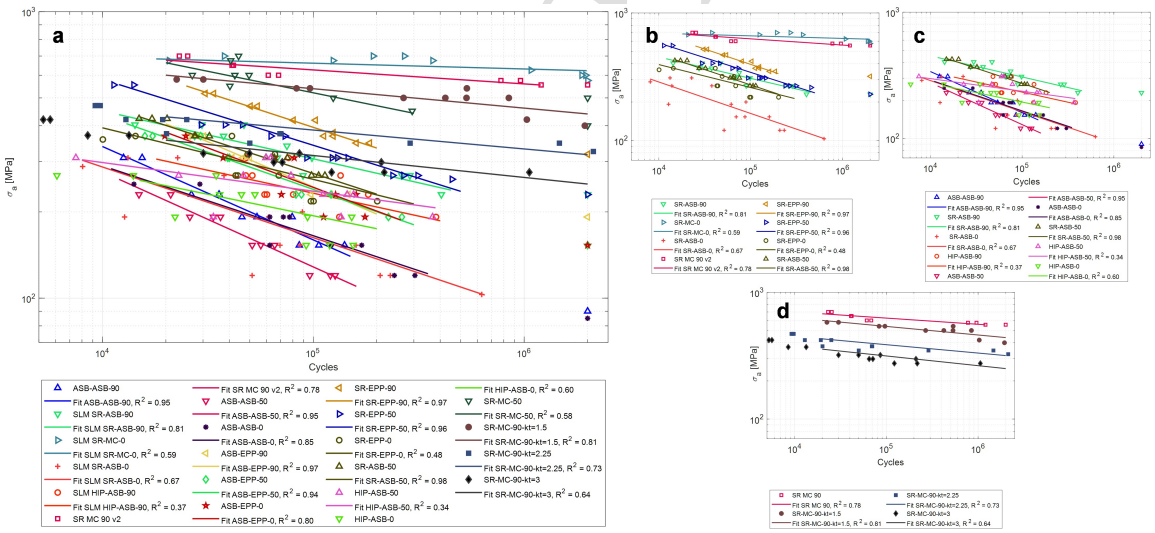

Figure 4: Fatigue stress-life curves of LPBF Ti-6Al-4V at all sample conditions (R=-1). a) Complete fatigue database for L-PBF Ti-6Al-4V. b) Fatigue performance of L-PBF Ti-6Al-4V in function of the building orientation and surface condition. c) Fatigue performance of L-PBF Ti-6Al-4V in function of different building orientation and different microstructures generated by volumetric treatments. d) Fatigue performance of L-PBF Ti-6Al-4V specimens with machined surface and different notch geometries.

Fatigue results of all the sample conditions are shown in Figure 4. The relationship between stress amplitude and cycles to failure is plotted in log-log scale. When studying the surface condition Figure 4-(b), it becomes clear that non-machined samples exhibit the lowest fatigue performance. Significant improvement is seen after electro plasma

polishing. The highest results are observed for machined samples. Comparing the influence of heat treatments, Figure 4-(c), shows that as-built samples exhibit the lowest performance and stress relieved samples the highest. The results of HIP samples lie in between these two conditions. Varying trends are seen on the influence of build orientation. In general, for all the microstructural conditions, vertically built samples performed better than inclined samples, followed by horizontal ones. Stress relieved and EPP samples also exhibit a similar trend. However, no significant variations are seen for as-built and EPP samples . Within the stress relieved and machined category, horizontal and vertical samples record the highest performance, followed by inclined ones. Furthermore, the influence of geometric discontinuities can be observed in Figure 4-(d). The fatigue life in low and high cycles regime was reduced in presence of notches with $k_t = 3.09$ batch showing the lowest fatigue behaviour.

Representative fracture surfaces for the stress relieved condition are shown in Figure 5. Cracks initiated from the surface and propagated towards the core for all the sample conditions. A rough surface can be seen for non-machined samples in Figure 5-a and d with unmolten powder particles sintered to the surface. A micro-notch effect is induced by the stress concentrators from this rough surface, leading to early crack initiation. A finer surface is obtained after the EPP operation and cracks initiated from the surface, as expected from samples with no obvious surface stress raisers. Figure 5-b and e show the fracture surfaces of an EPP sample. Fracture surfaces of machined samples in Figure 5-c and f reveal a very similar appearance as those of the EPP samples.

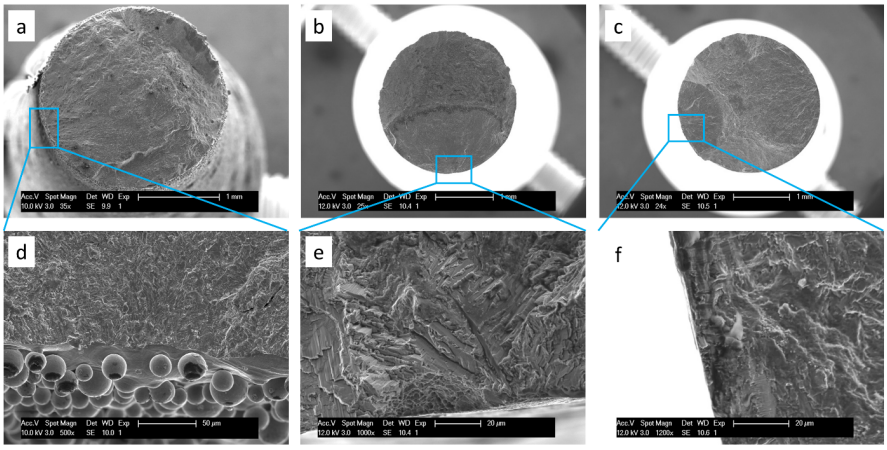

Figure 5: Fracture surfaces of stress relieved samples in non-machined (a) and (d), EPP (b) and (e), and machined (c) and (f) conditions

The fatigue database presented in Figure 4 has been extended with the Haigh's diagram presented in a previous study by Cutolo et al. [25] in which the detrimental impact of positive mean stresses have on L-PBF Ti-6Al-4V fatigue properties was presented. Two main behaviours were observed: on the one hand, for the machined and electro-polished coupons, the relation between stress amplitude and mean stress follows a linear Soderberg's, whereas for as-produced surfaces, a Walker's equation expresses the variation of the stress amplitude with the mean stress.

Component fatigue testing

Fatigue test results of the components are presented in Table 4 in terms of maximum applied load, number of cycles to complete failure and cycles to damage initiation. The number of cycles to failure was determined as the last complete cycle that the component could withstand before the destruction of the sample occurred.

Table 4: Overview of the component fatigue tests.

Test id.	1	2	3	4	5	6	7	8	9	10
Load level	12kN	12kN	12kN	14kN	14kN	10.8kN	10.8kN	10.8kN	14kN	12kN
Cycles to failure	113,000	99,000	105,000	59,000	58,000	190,500	173,000	157,000	60,500	118,500
Cycles to damage initiation	70,000	95,500	83,600	50,755	49,520	120,664	116,811	114,044	48,400	90,433

Figure 6 shows the evolution of the maximum and minimum displacement during a component fatigue test. As can be noticed, there is a large difference between the displacement at the final load cycle and the displacement at the cycle at which the minimum displacement starts to significantly decrease. This experimentally observed drop in stiffness, with as a consequence a decrease of the minimum displacement, has been considered as the point of damage initiation and early crack propagation.

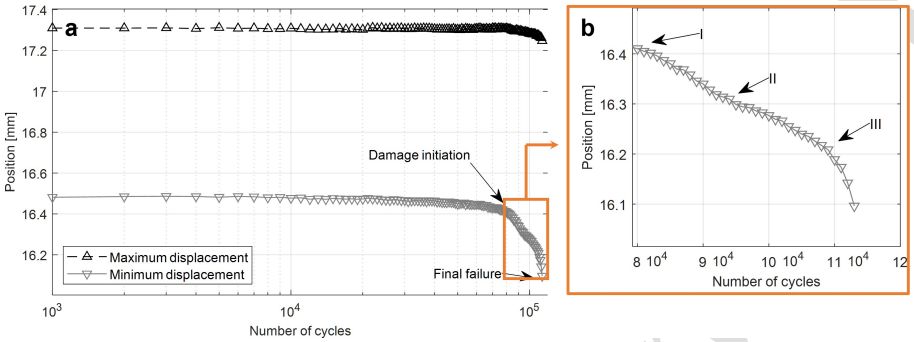

Figure 6: Representative maximum and minimum displacement evolution during component fatigue testing

More specifically, the cycle count at which the compliance, defined as the displacement amplitude normalized with the displacement amplitude at the 5000^{th} cycle, drops by 6%, has been considered as damage initiation point in this work. The experimentally observed number of cycles at damage initiation has been compared with the prediction as presented in the next section.

By looking at the evolution of the minimum displacement in function of the number of cycles to failure, it is possible to trace the damage evolution of the component. The crack initiate at the internal hole and propagates throughout the internal thin walled flange. Once it reached the bulky regions (Figure 1-(c) and (e)), the displacement rate changes (II in Figure 6-(b)), and multiple cracks were generated in proximity of the hardened cylinders. Once these secondary cracks propagated across the component, the final fracture occurred (Figure 6-(b) and Figure 7-(c)).

Post-fracture component analysis revealed that fatigue cracks always initiated at the top and bottom surfaces of the component internal hole (region I of Figure 1-(b)), and then propagated across the internal flange following a direction that is slightly inclined with respect to the building direction.

A typical crack path is presented in Figure 7-(a). Due to the poor surface quality of these regions, fatigue failures are prone to initiate at these locations. Figure 7-(b) shows representative fractured surfaces of the components around the hole with the red arrows indicating possible crack initiation locations.

The internal holes were not machined, therefore, their surfaces present the typical morphology resulting from the L-PBF process. The top part of the hole presents a high surface roughness characterized by a large amount of partially molten particles. Moreover, at this location, the surface presents several imperfections resulting from the dross formation during the manufacturing of non-supported down-facing surfaces. In particular, the top-right and top-left corners, Figure 7-(b), present both lack of material that result in the undesirable formation of sharp notches that can act as stress raisers which facilitated the crack onset.

The bottom surface, on the other hand, presents the typical morphology of slightly inclined up-facing surfaces characterized by the staircase effect. In this case, the fatigue cracks might initiate at the inter-layer notches between two successive layers, as indicated by the orange arrows on Figure 7-(b).

Component fatigue prediction

Figure 8-a shows the maximum principal stress for a region of interest of the tested component under a $1.5kN$ load. The highest principal stresses are found near the hole in the component (region I in Figure 1-(b)), while a more extensive zone of high stresses (80% of the absolute maximum principal stress in the model) is found in region II. While surface conditions (orientation between principal stress and print layers, as well as surface roughness conditions) are different in regions I and II, a first analysis with the Durability solver indicates that region I is in fact the

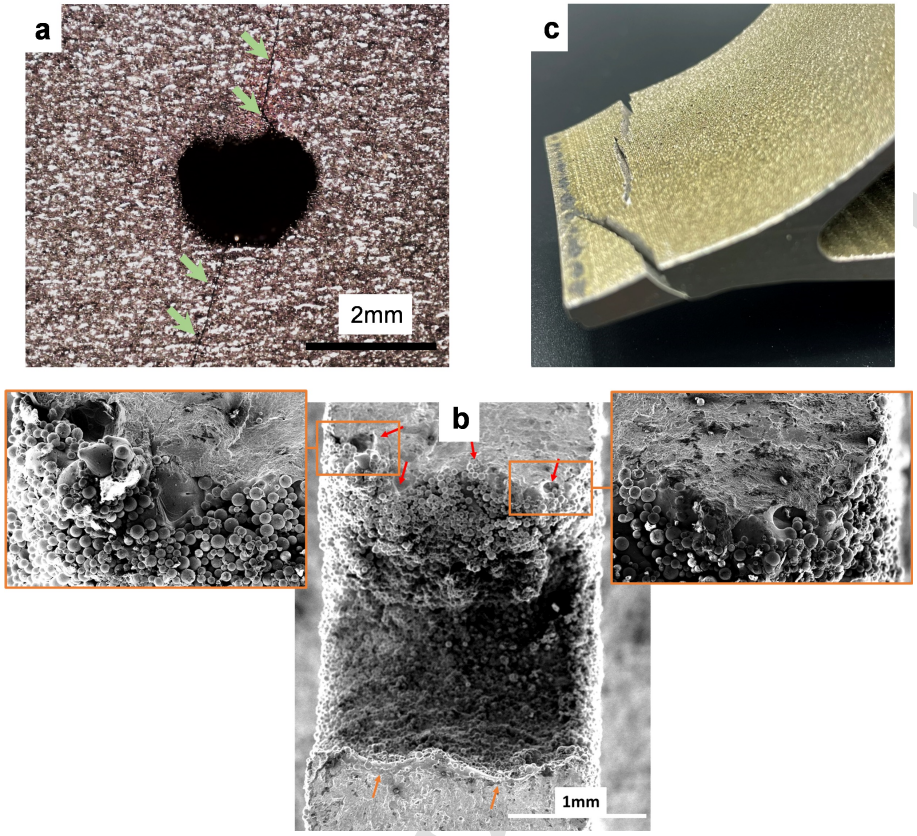

Figure 7: (a) Optical microscopy of the component internal flange after a fatigue test. The green arrows indicate two cracks initiating at the hole down-facing and up-facing surfaces. The black arrow indicates the building direction. (b) SEM images of the component fractured surface: crack initiated both at the top and bottom surface of the internal hole; top-right corner and top-left corner presenting lack of material due to dross formation. (c) Final fracture of the demonstrator.

critical area in terms of fatigue failure as the stress amplitude is higher while the surface condition is less favourable for fatigue.

In order to obtain a higher resolution of the stress concentrations surrounding the hole, a sub-modelling approach was used to build a high-fidelity model of region I. The macro-model and micro-model were linked through the displacement fields at the boundaries of the micro-model.

A close-up of the micro-model under similar loading conditions as the macro-model is shown in Figure 8-b. This sub-model consists of 210,000 CHEXA(20) quadratic elements with average element size of $35\mu m$. The obtained maximal stress is close to the stresses obtained in the macro-model. However, due to the increased mesh density, a better approximation of the stress field away from the surface can be obtained, which will be exploited in compensating for notch effects in the durability analysis.

Figure 8-(c) shows the outcome of the Durability analysis using the custom designed fatigue prediction model on the sub-model, at a load amplitude of $4.86kN$ and an R-ratio of 0.1. The results show a very low cycle count of 1,500 cycles at the most critically loaded element in the model. However, it can also be seen that a strong gradient exists near the surface, where lifetime quickly increases away from the surface. It is well-known that for strong stress gradients (or notches) compensation measures must be implemented to avoid underestimating fatigue life due to sharply concentrated stresses. A critical distance compensation method was implemented in a post-processing scenario, based on results from notched coupons [28] (pre-print article, under revision FFEMS). Lifetime of the component was then estimated at the critical distance normal to the surface at the highest stress concentration, resulting in an estimated lifetime of approximately 100,000 cycles (compared to the original 1,500 cycles at the surface stress

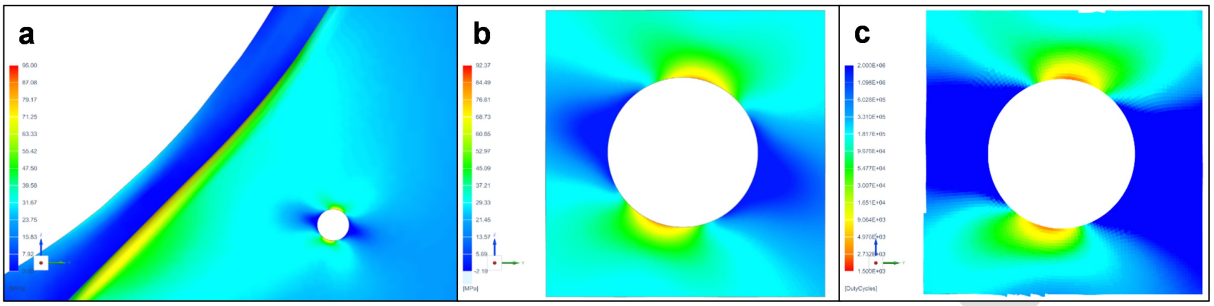

Figure 8: (a) Component principal stress field at the critical locations for 1.5kN load, (b) Sub-model of component critical area under a 1.5kN macroscopic load. (c) Durability prediction for a 4.86kN load amplitude at $R = 0.1$, accounting for as-built surface roughness on the surface and stress-relieved material condition

concentration).

Validation of component fatigue life prediction

From a comparison of Figure 7-(a) and Figure 8 it can be noticed that the Durability solver can properly isolate the damage initiation for the component accounting for the poor surface quality of the as produced hole. Moreover, the simulation results also clearly indicate the path that the cracks will follow during the propagation phase. In fact, Figure 8-(c) shows that the two crack initiation points are on a direction that is inclined with respect to the vertical direction.

Figure 9 shows the computationally predicted SN-curve (using the Specialist Durability solver) and its confidence interval, overlaid on top the experimental test results of the campaign.

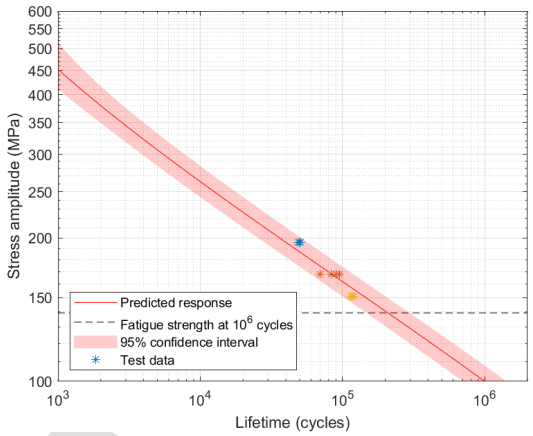

Figure 9: Computational prediction of SN-curve in Region I of the component and the confidence interval on the prediction, overlaid with experimental data points

The results show a very good correspondence between the numerical predictions and the experimental data points. All test results fall within the confidence interval of the numerical simulations. Note that the stress amplitudes for the experimental data points were obtained by a linear rescaling of the stresses (critical distance compensated) for the 4.86kN load amplitude (red asterisks in Figure 9), based on the applied load levels. However, as the critical distance compensation is in fact a function of the component lifetime, it can be expected that the calculated stress level for low lifetimes (blue asterisk) is slightly overestimated, while for long lifetimes (yellow asterisks) the stress level is underestimated. More advanced critical distance compensation (work in progress) will result in an even better match between simulation and experiment.

Conclusions

This work presents a validated approach for predicting the failure location and the fatigue life of metal components produced by LPBF based on sample data, FE-simulations and machine learning. More specifically, an industrially relevant component with several realistic features has been produced by LPBF in Ti-6Al-4V and was tested under dynamic loading as a real validation for the fatigue prediction model. The following conclusions can be made:

- To capture all relevant fatigue influencing factors, a comprehensive database with fatigue properties of standardized samples under different conditions is required. These conditions depend on the final application. In this study they include: build orientation, heat treatment, post-process machining operation, notch and stress-gradient effect.
- It takes considerable effort to create such sample fatigue database, but with the advantage that such database can be used to predict the fatigue life of components produced on the same AM machine using the same material and processing conditions, and thus avoiding the very time- and cost-expensive fatigue testing of large complex components.
- Machine-learning can be an effective tool to use all sample fatigue data available as input to estimate fatigue performance for sample conditions that were not tested.
- FE-based stress calculation is required as input for any fatigue life prediction method, and is fairly straightforward as for any AM part a suitable CAD file is always available.
- In the present work, the effect of the stress-gradient on fatigue life could be accurately accounted for using the critical distance method.
- The failure location of the industrially relevant Ti-6Al-4V component could be accurately predicted in this work. This is very interesting on its own, as it can allow LPBF users to decide for post-machining of only those areas that are predicted as sensitive locations for crack initiation, hence reducing the post-processing costs significantly compared to full component machining.
- The fatigue life prediction tool was also able to predict the number of cycles to failure within a 95% confidence interval.

Appendix I

Machine learning - The Gaussian process

A Gaussian process $\mathcal{GP}$ is defined as a collection of random variables indexed by some continuous input vector $\boldsymbol{x}$ of dimension d such that for any finite set of input vectors the corresponding random variables are jointly Gaussian distributed [29]. In other words, the Gaussian process might be pictured as a multivariate Gaussian distribution whose dimensionality, mean vector, and covariance matrix are functions of a set of input vectors. For a single input vector, the Gaussian process produces a normal variable such that $\mathcal{GP}(\boldsymbol{x}) \sim \mathcal{N}(\mu(\boldsymbol{x}), \sigma^2(\boldsymbol{x}))$. For an extension to the multidimensional case let $\boldsymbol{X} = [\boldsymbol{x}_1^T, ..., \boldsymbol{x}_n^T]$, where n defines the size of the set. Then the Gaussian process produces an n-dimensional output vector, which is jointly Gaussian distributed such that $\mathcal{GP}(\boldsymbol{X}) \sim \mathcal{N}(\boldsymbol{m_F}(\boldsymbol{X}), \boldsymbol{K_F}(\boldsymbol{X}))$. Let $\boldsymbol{y} = [y_1, ..., y_n]^T$ be a vector containing experimental observations. If a Gaussian process is to be used to model a relation to $\boldsymbol{X}$, $\boldsymbol{y}$ is considered a realization of n random variables. They are divided into a $\mathcal{GP}$ and a noise term $\boldsymbol{E}$ such that

$$\boldsymbol{Y} \sim \mathcal{GP}_{\boldsymbol{Y}} + \boldsymbol{E}|\mathcal{GP}_{\boldsymbol{Y}}. \tag{2}$$

Herein, $\boldsymbol{E}$ can have an arbitrary pdf and is also referred to as likelihood function. Thus, the experimental findings $\boldsymbol{y}$ are considered a draw from a multivariate Gaussian distribution with added noise. It is pointed out that only $\boldsymbol{Y}$ is observable in experiments, not the output of $\mathcal{GP}$ or $\boldsymbol{E}$.

In case $\boldsymbol{E}$ is assumed to be a normally distributed random variable with zero mean and covariance matrix $\sigma_E \boldsymbol{I}$, Equation (2) results in

$$\varphi_{\boldsymbol{Y}} \sim \mathcal{N}(\boldsymbol{g_Y}|\boldsymbol{m_Y}(\boldsymbol{X}), \boldsymbol{K_Y}(\boldsymbol{X})) \cdot \mathcal{N}(\boldsymbol{y}|\boldsymbol{g_Y}, \sigma_E \boldsymbol{I}), \tag{3}$$

where $\boldsymbol{g}_{\boldsymbol{Y}}$ is a draw from the $\mathcal{GP}$ that is used to model $\boldsymbol{Y}$ and $\boldsymbol{I}$ is the identity matrix of size $n \times n$. It is pointed out that Gaussians are closed under multiplication. The product of two Gaussians is another (un-normalized) Gaussian.

$\boldsymbol{m}$ and $\boldsymbol{K}$ are constructed using mean functions m and covariance functions k, also referred to as kernel, such that

$$[\boldsymbol{m}]_i = m(\boldsymbol{x}_i) \quad \text{and} \quad [\boldsymbol{K}]_{ij} = k(\boldsymbol{x}_i, \boldsymbol{x}_j). \tag{4}$$

The parameters required in these functions are referred to as hyper-parameters. m can be freely selected, but the resulting $\boldsymbol{K}$ must be positive semi-definite. Covariance functions most often work on the difference between input vectors $(\boldsymbol{x}_i - \boldsymbol{x}_j)$ or on their similarity $(\boldsymbol{x}_i \cdot \boldsymbol{x}_j)$. If those operations are not defined for the input vectors, they need to be mapped to another space where those operations are indeed defined. For details on how to construct kernels and how to analyse their properties, the reader is referred to [29]. See [30] and references therein on how to choose a covariance function.

So far, the Gaussian process has been used to produce joint distributions. To be of practical use, it is aimed at obtaining the output y corresponding to some new input $\boldsymbol{x}$ based on some experimental data $\boldsymbol{X}$ and $\boldsymbol{y}$. To this end, the joint distribution $\varphi_{\boldsymbol{Y},Y}$ is conditioned to obtain the conditional distribution $\varphi_{Y|\boldsymbol{Y}}$. If the added noise is assumed to be Gaussian as detailed above, closed form solutions are available and the expected mean and the variance of $Y|\boldsymbol{Y}$ read

$$\mathbb{E}\left[Y|\boldsymbol{Y}\right] = \mu_Y(\boldsymbol{x}) + \boldsymbol{k}^T(\boldsymbol{X}, \boldsymbol{x})(\boldsymbol{K}_{\boldsymbol{Y}}(\boldsymbol{X}) + \sigma_E^2 \boldsymbol{I})^{-1}(\boldsymbol{y} - \boldsymbol{m}_{\boldsymbol{Y}}(\boldsymbol{X})) \tag{5}$$

and

$$\mathbb{V}\left[Y|\boldsymbol{Y}\right] = k(\boldsymbol{x}, \boldsymbol{x}) - \boldsymbol{k}^T(\boldsymbol{X}, \boldsymbol{x})(\boldsymbol{K}(\boldsymbol{X}) + \sigma_E^2 \boldsymbol{I})^{-1}\boldsymbol{k}(\boldsymbol{X}, \boldsymbol{x}), \tag{6}$$

respectively. Therein, $\boldsymbol{k}$ is a vector of length n that is obtained when evaluating the covariance function for the new input combined with all other input. Furthermore, the mean value is called a linear predictor since it linearly combines the training data points.

Gaussian process regression

From experiments on uni-axially loaded specimen presented in Figure 4, the raw input vector

$$\boldsymbol{x}_{\text{raw}} = [x, r, \psi, t_{\text{vol}}]^T \tag{7}$$

and the corresponding load cycles until failure are available. Therein, r defines the surface roughness, ψ signifies the angle between the printing direction and the maximal principal stress direction, and

$$t_{\text{vol}} \in \{\text{as-built (ASB), hot isostatic pressing (HIP), stress release (SR)}\} \tag{8}$$

is a categorical parameter indicating the volume treatment applied. For 18 different combinations of r, ψ, and t_{vol} SN curves have been experimentally determined by varying only x. The different settings and properties distinctively change the fatigue characteristics. For such cases, where there is additional knowledge available, the Gaussian process model can be vastly advantageous. A kernel can be formulated based on little knowledge to capture the trends in the data. Unfortunately, the data does not contain enough run-outs to employ a Gaussian process to predict the endurance limit. Hence, the run-outs are disregarded in the present study.

Transformation of input vector

Any transformation of the input needs to conserve the properties of covariance functions as mentioned in the previous paragraph. Then, transforming the input can be understood as defining a new kernel. First of all, since $\boldsymbol{x}_{\text{raw}}$ contains continuous as well as discrete variables, the map $\{$ ASB, HIP, SR$\} \rightarrow \{0,1\}\times\{0,1\}\times\{0,1\}$ given by $t_{\text{vol}} \mapsto \boldsymbol{t}_{\text{vol}}$ is introduced, where a 1 signifies the applied volume treatment [30]. Secondly, the common logarithm of r is taken to more evenly distribute the values. Thirdly, the continuous parameters x, $\log_{10} r$ and ψ are subtracted by their respective mean and subsequently divided by their respective standard deviation to obtain the standardized quantities $\tilde{x}$, $\log_{10} \tilde{r}$, and $\tilde{\psi}$, respectively. Upon this standardization an easy prior with zero mean can be assumed. Thus, a 6-dimensional

input vector

$$\tilde{\boldsymbol{x}} = \left[\tilde{x}, \log_{10}\tilde{r}, \tilde{\psi}, \boldsymbol{t}_{\text{vol}}^T\right]^T \tag{9}$$

is generated for every data point.

Definition of kernel

Here, a kernel is presented based on the simple assumption that life is a monotonically decreasing linear function of $\tilde{x}$ and $\log_{10}\tilde{r}$. This means that an increased distance between data points does not result in a loss of covariance but in an increase thereof. For example, if we were to predict the life of a specimen based on a single measurement, we would be more certain life decreased the higher the stress value (or surface roughness value) was relative to the single data point. The overall linear trend is captured by

$$k_1(\tilde{\boldsymbol{x}}_i, \tilde{\boldsymbol{x}}_j) = \begin{bmatrix} \tilde{x}_i \\ \log_{10}\tilde{r}_i \end{bmatrix} \cdot \begin{bmatrix} \theta_1^2 & \theta_1\theta_2 \\ \theta_1\theta_2 & \theta_2^2 \end{bmatrix} \begin{bmatrix} \tilde{x}_j \\ \log_{10}\tilde{r}_j \end{bmatrix} \tag{10}$$

introducing the two hyper-parameters θ_1 and θ_2. The smaller their values are, the less sensitive the output is to a change of the corresponding input variables. To locally allow for a deviation from this linear trend, the two functions

$$k_2(\boldsymbol{x}_i, \boldsymbol{x}_j) = \left(\tilde{x}_i\ \tilde{x}_j\right)\theta_3^2 \exp\left[-\frac{1}{2}\Delta\boldsymbol{x}^T \operatorname{diag}\left(0, 0, \theta_4^{-2}, \theta_5^{-2}, \theta_6^{-2}, \theta_7^{-2}\right)\Delta\boldsymbol{x}\right] \tag{11}$$

and

$$k_3(\boldsymbol{x}_i, \boldsymbol{x}_j) = \left(\log_{10}\tilde{r}_i\ \log_{10}\tilde{r}_j\right)\cdot\theta_8^2 \exp\left[-\frac{1}{2}\Delta\boldsymbol{x}^T \operatorname{diag}\left(0, 0, \theta_9^{-2}, \theta_{10}^{-2}, \theta_{11}^{-2}, \theta_{12}^{-2}\right)\Delta\boldsymbol{x}\right] \tag{12}$$

are formulated, where $\Delta\boldsymbol{x} = \boldsymbol{x}_i - \boldsymbol{x}_j$ and $\operatorname{diag}(\bullet)$ defines a diagonal matrix containing the different length scales. These two covariance functions can be seen as a linear model, much as in Equation (10), but with the hyper-parameters describing the linear trend replaced by a squared-exponential kernel. θ_3 and θ_4 signify signal variance and θ_4-θ_7 as well as θ_9-θ_{12} define length-scales. In the process of maximizing the marginal likelihood, large length-scales will be identified for negligible input dimensions. In k_2 and k_3, the first two diagonal elements are set to zero to ensure monotonicity when the stress or surface roughness varies. Far away from any training data, the contribution of the squared exponential will approach zero and the linear trend will be described solely by k_1. Next, the kernel is refined by

$$k_4(\boldsymbol{x}_i, \boldsymbol{x}_j) = \theta_{13}^2 \exp\left[-\frac{1}{2}(\tilde{\psi}_i - \tilde{\psi}_j)\theta_{14}^{-2}(\tilde{\psi}_i - \tilde{\psi}_j)\right] \tag{13}$$

and

$$k_5(\boldsymbol{x}_i, \boldsymbol{x}_j) = \theta_{15}^2 \exp\left[-\frac{1}{2}\Delta\boldsymbol{x}^T \operatorname{diag}\left(0, 0, 0, \theta_{16}^{-2}, \theta_{17}^{-2}, \theta_{18}^{-2}\right)\Delta\boldsymbol{x}\right] \tag{14}$$

to smoothly capture the covariances when altering ψ and t_{vol}. θ_{13} and θ_{15} are signal variances. For insignificant input dimensions large values for the length-scales θ_{14} and θ_{16}-θ_{18} are identified in the optimization procedure. Finally,

$$k_6(\boldsymbol{x}_i, \boldsymbol{x}_j) = \theta_{19}^2 \delta_{ij} \tag{15}$$

is employed to describe the scatter by the independent noise parameter θ_{19}. The kernel actually used in the Gaussian process regression results from summing up the six different contributions. Altogether, 19 hyper-parameters are required which might seem a lot but they are used to compute $n_{\text{obs}}^2/2$ different entries of the covariance matrix. Moreover, 18 standard linear regression models would amount to 53 parameters. It is noted that the squared exponentials could not be replaced by less smooth covariance functions from the Matérn class, for example, which is believed to be due to the noisy and scarce data allowing only for the identification of smooth trends.

Identification of hyper-parameters

To identify the hyper-parameters, a variation of the *leave-one-out cross-validation* [29] is applied to balance data representation and generalization to new input. From the 18 SN-curves of Figure 4-(a) (excluding data for notched

specimens), 18 different training data sets are created, each consisting of 17 SN-curves. Then, the hyper-parameters are selected that globally maximize the sum of the 18 likelihoods. The obtained hyper-parameters listed in Table 5 result in a likelihood of −1146.

Table 5: Hyper-parameters of the presented kernel identified for Ti-6Al-4V data without run-outs.

θ_1	θ_2	θ_3	θ_4	θ_5	θ_6	θ_7
$6.23 \cdot 10^{-1}$	$5.64 \cdot 10^{-1}$	$1.29 \cdot 10^{-1}$	$3.28 \cdot 10^{0}$	$5.72 \cdot 10^{0}$	$1.36 \cdot 10^{4}$	$2.79 \cdot 10^{-1}$
θ_8	θ_9	θ_{10}	θ_{11}	θ_{12}	θ_{13}	θ_{14}
$2.59 \cdot 10^{-1}$	$3.04 \cdot 10^{-4}$	$1.32 \cdot 10^{-2}$	$1.62 \cdot 10^{2}$	$9.36 \cdot 10^{-4}$	$3.32 \cdot 10^{0}$	$7.03 \cdot 10^{0}$
θ_{15}	θ_{16}	θ_{17}	θ_{18}	θ_{19}		
$2.97 \cdot 10^{-1}$	$4.90 \cdot 10^{-3}$	$5.26 \cdot 10^{1}$	$1.70 \cdot 10^{0}$	$2.97 \cdot 10^{-1}$		

Based on the values obtained for θ_1 and θ_2 it can be stated that a clear non-stationary trend is identified for the influence of the stress and surface roughness on life. Likewise, θ_3 and θ_8 are in the same order of magnitude such that the slopes will vary locally. But since θ_4- θ_6 are relatively large, the covariance captured by k_2 is dominated by θ_7. The short length-scale θ_9 results from the very noisy data such that no smooth trend is present. The small values of θ_{10} and θ_{12} suggest a high relevance of the corresponding heat treatments in the covariance of Y at different surface roughness values. θ_{14} appears to be large in comparison to the other length-scales but it reflects that ψ has a bigger range. Moreover, large values are obtained for the length-scales θ_6, θ_{11}, and θ_{17}, which all correspond to the volume treatment HIP effectively removing this input dimension. Thus, in predictions it will only matter if the specimen received any volume treatment at all.

To give a more intuitive examination of the kernel, the ordinary least-squares method is applied to both, the experimental data and the predicted mean of life from the Gaussian process determining the intercept c_0 as well as the slope c_1. The results of that procedure are shown in Table 6. Therein, the standard deviations of a prediction σ_p are given as well. The resulting mean values of σ_p are 0.23 and 0.31, respectively. This means that, as could be expected, the 18 different linear fits are closer to the data as the Gaussian process model, which 'explains' more of the data with noise. The kernel identifies two different slopes that depend on if a volume treatment was applied. This observation is in line with remarks made above about the values of the identified hyper-parameters. Apparently, the coupling between surface roughness and stress captured by k_1 is too weak to be noticeable here. The slight differences in slopes are erased by rounding off.

Furthermore, it seems to be instructive to study the cases #11 and #18, two SN-curves with distinct differences between the obtained parameters given in Table 6. The raw data, the respective least-squares fit, the prediction of the Gaussian process, and the respective 95% prediction intervals for the two cases are depicted in Figure 10. In Figure 10-(a) the data shows little scatter and accordingly the least-squares fit leads to small uncertainties of predicted values. In contrast, the Gaussian process predicts a distinctively larger variance as an average of the total noise in the data is deduced and used in predictions. In other words, the Gaussian process also 'knows' the scatter of all other data and it is concluded that #11 only constitutes a 'lucky' draw from a much noisier distribution. Figure 10-(b) shows the data of SN-curve #18, which is considered a rather improbable draw from the underlying distribution following from the given kernel. The deviation from the rest of the data is thus explained by noise. In comparison to SN-curve #11, it is shifted keeping the slope roughly constant. Although in this case, a single linear fit leads to completely different conclusions, it might be arguable that in the process of data analysis the three data points with the highest life in Figure 10-(b) could have been excluded from the fitting process with a linear model. Then, the obtained slope and intercept would be more similar to the predictions of the Gaussian process.

Table 6: Results of the ordinary least-squares method performed on the data and the Gaussian process outputs.

	Data			Gaussian process			Differences in %		
#	c_0	c_1	σ_p	c_0	c_1	σ_p	Δc_0	Δc_1	$\Delta\sigma_p$
1	12.00	-3.18	0.23	10.64	-2.54	0.31	12.8	25.1	25.8
2	10.91	-2.81	0.07	10.38	-2.54	0.31	5.2	10.6	77.0
3	11.48	-2.95	0.10	10.74	-2.54	0.31	6.9	16.1	68.5
4	11.37	-2.69	0.19	10.72	-2.54	0.30	6.1	5.8	38.8
5	12.55	-3.21	0.18	10.87	-2.54	0.30	15.5	26.3	40.9
6	12.44	-3.12	0.06	11.08	-2.54	0.31	12.3	22.8	79.4
7	12.92	-3.56	0.31	12.68	-3.47	0.31	1.9	2.7	0.3
8	12.57	-3.24	0.41	13.14	-3.47	0.31	4.3	6.6	33.3
9	11.11	-2.58	0.26	13.25	-3.47	0.31	16.1	25.6	16.5
10	11.05	-2.79	0.32	12.72	-3.47	0.30	13.1	19.6	6.5
11	14.91	-4.06	0.05	13.44	-3.47	0.30	11.0	17.1	82.4
12	17.17	-4.91	0.21	13.48	-3.47	0.30	27.4	41.6	32.3
13	17.54	-5.24	0.43	13.24	-3.47	0.30	32.5	51.1	40.7
14	16.06	-4.38	0.11	13.62	-3.47	0.30	17.9	26.3	64.9
15	15.41	-4.01	0.06	13.83	-3.47	0.30	11.4	15.6	81.6
16	53.54	-17.08	0.50	15.32	-3.47	0.31	249.4	392.5	61.1
17	16.52	-4.26	0.23	14.37	-3.47	0.31	15.0	22.8	28.0
18	51.88	-16.76	0.39	14.79	-3.47	0.31	250.8	383.3	24.6
mean			0.23			0.31	39.42	61.74	44.58

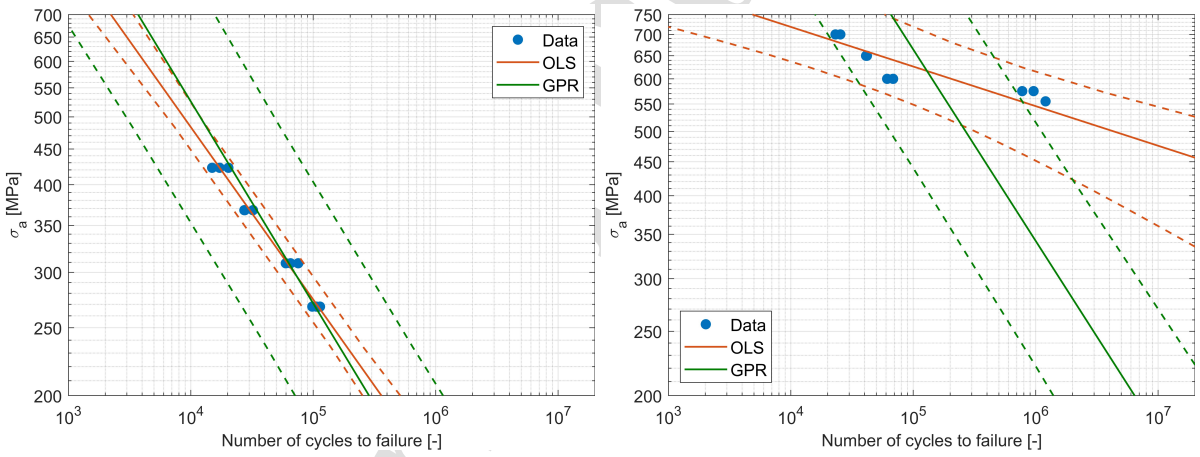

(a) #11 (b) #18

Figure 10: The SN-curves #11 and #18 are depicted along with an ordinary least-squares fit, the Gaussian process predictions, and the 95% prediction intervals.

Appendix II

Definition of the critical distance

The experimental campaign included an investigation on notch sensitivity of Ti-6Al-4V specimens produced by L-PBF. In particular, samples with three different notch geometries (Figure 1-(a)) were investigated.

In order to understand the fatigue behaviour of notched specimens with respect to the plain coupons it is important to evaluate the local stress distribution in the proximity of the notch root. In this regard, linear elastic FE analysis was

performed under axial loading condition. Due to the double symmetry, the numerical models consist of one fourth of the geometry presented in Figure 1-(b). The numerical simulations results for the three different notch geometries indicate that the three discontinuities generate a stress re-distribution across the smallest cross section with a stress concentration at the notch root. An example of the FE numerical simulation results is presented in Figure 11-(a), in which the geometry with the smallest radius, i.e. $\rho = 0.25mm$, was analysed.

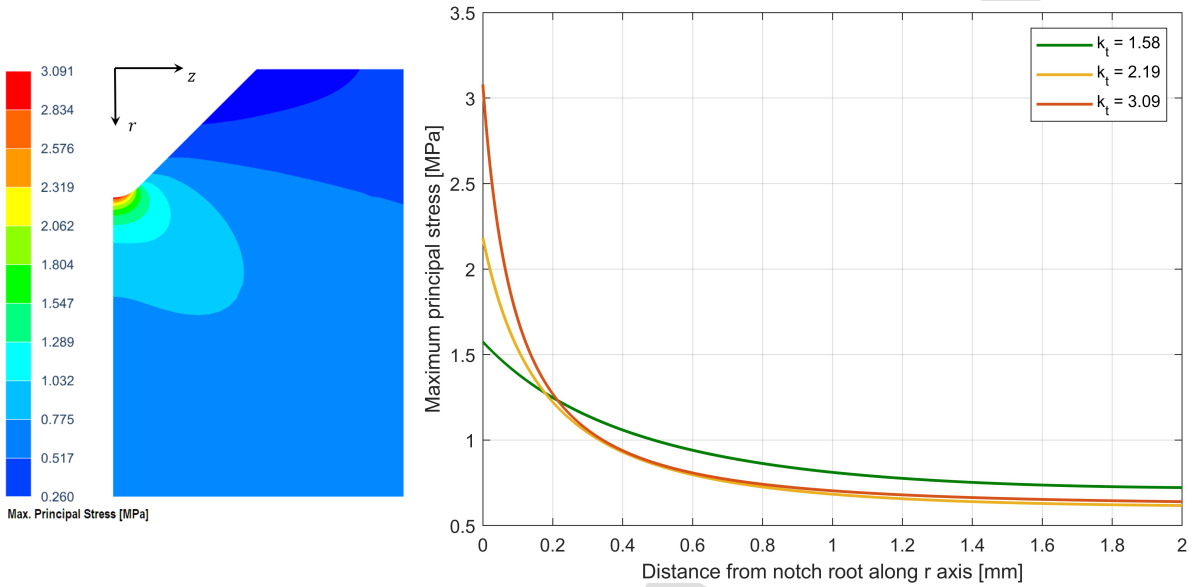

Figure 11: (a) normalized principal stress distribution for $k_t = 3.09$; b) normalized principal stress in function of the distance from the notch root for the three notched geometries

Figure 11-(a) shows the principal stress distribution calculated for an applied load that generate a nominal stress of $1MPa$ across the smallest cross section. The graphs in Figure 11-(b) show the maximum principal stresses in function of the distance from the notch root towards to the centre of the model along the radial direction for the three notch geometry (direction r indicated in Figure 11-(a)). By dividing the maximum value of the maximum principal stress by the nominal stress across the smallest section it was possible to estimate the stress concentration factor k_t for the three notch geometries, i.e. $k_t = 1.58, k_t = 2.19, k_t = 3.09$, corresponding to the notch radii of $1.50mm, 0.50mm, 0.25mm$, respectively.

As presented in Figure 11-(b), the three notch radii generate different stress distributions with $\rho = 1.50mm$ generating a smoother transition from the peak stress to the stress plateau if compared to $\rho = 0.50mm$ and $\rho = 0.25mm$. On the contrary the latter two geometries induce similar stress distributions with a steeper transition from the peak stress to the stress plateau. The curves presented in Figure 11-(b) have been fitted with 2^{nd} degree polynomial rational functions of the type presented by eq. 16 using non-linear least square fitting in which the variable r represents the distance from the notch root along the axis r of Figure 11-(a).

$$\sigma_1(r) = \frac{p_1 r^2 + p_2 r + p_3}{r^2 + q_1 r + q_2} \tag{16}$$

The function expressed by eq 16 for the smaller notch radius ($\rho = 0.25mm, kt = 3.09$) has been used to evaluate the critical distance using the line method as:

$$\sigma_{eff} = \frac{1}{2l_0} \int_0^{2l_0} \sigma_1(r) dr \tag{17}$$

where σ_{eff} is the effective stress that generates the failure, l_0 is the critical distance, σ_1 is the principal stress, r represents the distance from the notch root. In the LM the stress is determined by averaging along a line L starting at

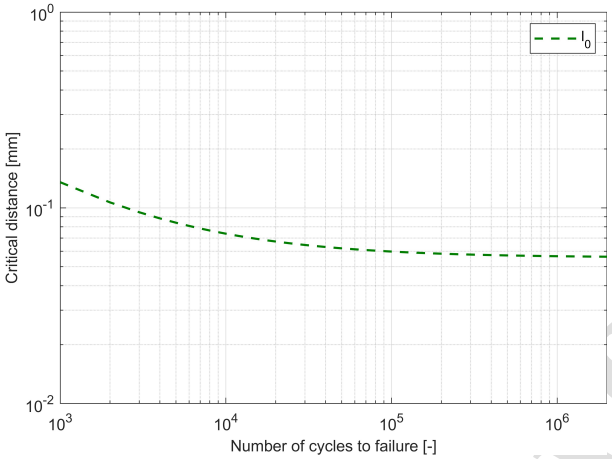

Figure 12: Critical distance in function of the number of cycles to failure

the notch-root. The length of this line is related to the critical distance by the relation: $L = 2l_0$ [31].

In particular, the critical distance has been evaluated using the TCD formulated with the line method (i.e. eq. 17) in the entire fatigue life range as proposed by Susmel and Taylor [32]. The authors re-formulate the TCD so as to predict notch components' fatigue life in the low, medium and high cycle regime. According to this procedure it is possible to define the critical distance in function of the number of cycles to failure. To achieve this, two calibration SN curves are needed: one generated for plain, non-notched samples and one obtained by testing notched specimens. For the present study the SN curves of plain and $k_t = 3.09$ specimens were considered as calibration curves. The relation between critical distance and the number of cycles to failure has been expressed as:

$$l_0(N_f) = A + \frac{B}{N_f^C} \tag{18}$$

with $A = 0.056$, $B = 6.704$, and $C = 0.642$. The results are presented in Figure 12 in which an asymptotic tendency of l_0 can be observed with the increase of N_f. The function expressed by eq. 18 has been used to compensate for the stress gradient generated by the hole in the internal flange of the component. In particular, given l_0 for the entire fatigue life range (i.e. $10^3 - 2 \cdot 10^6$), it was possible to calculate the effective stress σ_{eff} via eq. 17 in function of the number of cycles to failure.

Acknowledgement

The authors would like to acknowledge the financial support of SIM (Strategic Initiative Materials in Flanders) and VLAIO (Flemish government agency, Flanders Innovation & Entrepreneurship) through the M3-FATAM project (*HBC*.2016.0446), part of the MacroModelMat (M3) research program, coordinated by Siemens (Siemens Digital Industries Software, Belgium).

Highlights

- A large database consisting of the different fatigue performance of L-PBF Ti-6Al-4V coupons in function of different combinations building orientation, heat treatments, and surface treatments, is presented.
- The database is used as training dataset for a machine learning algorithm that, in combination with FE simulation, has been adopted to build a simulation-based fatigue prediction tool.
- The tool has been used to predict the fatigue performance of an L-PBF Ti-6Al-4V part. The predictions were validated by experimental fatigue testing, providing accurate life estimation.

References

[1] K. Kempen, L. Thijs, J. Van Humbeeck, J.-P. Kruth, Processing Al-Si-10Mg by selective laser melting: parameter optimisation and material characterisation, Materials Science and Technology 31 (8) (2015) 917–923.

[2] L. Thijs, F. Verhaeghe, T. Craeghs, J. Van Humbeeck, J.-P. Kruth, A study of the microstructural evolution during selective laser melting of Ti-6Al-4V, Acta materialia 58 (9) (2010) 3303–3312.

[3] C. Wang, X. Tan, E. Liu, S. B. Tor, Process parameter optimization and mechanical properties for additively manufactured stainless steel 316l parts by selective electron beam melting, Materials & Design 147 (2018) 157–166.

[4] S. Liu, Y. C. Shin, Additive manufacturing of Ti-6Al-4V alloy: A review, Materials & Design 164 (2019) 107552.

[5] B. Van Hooreweder, D. Moens, R. Boonen, J.-P. Kruth, P. Sas, Analysis of fracture toughness and crack propagation of Ti-6Al-4V produced by selective laser melting, Advanced Engineering Materials 14 (1-2) (2012) 92–97.

[6] M. Simonelli, Y. Y. Tse, C. Tuck, Effect of the build orientation on the mechanical properties and fracture modes of slm ti–6al–4v, Materials Science and Engineering: A 616 (2014) 1–11.

[7] B. Van Hooreweder, Y. Apers, K. Lietaert, J.-P. Kruth, Improving the fatigue performance of porous metallic biomaterials produced by selective laser melting, Acta biomaterialia 47 (2017) 193–202.

[8] J. Günther, S. Leuders, P. Koppa, T. Tröster, S. Henkel, H. Biermann, T. Niendorf, On the effect of internal channels and surface roughness on the high-cycle fatigue performance of ti-6al-4v processed by slm, Materials & Design 143 (2018) 1–11.

[9] B. Vayssette, N. Saintier, C. Brugger, M. Elmay, E. Pessard, Surface roughness of ti-6al-4v parts obtained by slm and ebm: Effect on the high cycle fatigue life, Procedia engineering 213 (2018) 89–97.

[10] A. Fatemi, R. Molaei, S. Sharifimehr, N. Phan, N. Shamsaei, Multiaxial fatigue behavior of wrought and additive manufactured ti-6al-4v including surface finish effect, International Journal of Fatigue 100 (2017) 347–366.

[11] A. Fatemi, R. Molaei, J. Simsiriwong, N. Sanaei, J. Pegues, B. Torries, N. Phan, N. Shamsaei, Fatigue behaviour of additive manufactured materials: An overview of some recent experimental studies on ti-6al-4v considering various processing and loading direction effects, Fatigue & Fracture of Engineering Materials & Structures 42 (5) (2019) 991–1009.

[12] J. Pegues, M. Roach, R. S. Williamson, N. Shamsaei, Surface roughness effects on the fatigue strength of additively manufactured ti-6al-4v, International Journal of Fatigue 116 (2018) 543–552.

[13] A. K. Singla, M. Banerjee, A. Sharma, J. Singh, A. Bansal, M. K. Gupta, N. Khanna, A. Shahi, D. K. Goyal, Selective laser melting of Ti-6Al-4V alloy: Process parameters, defects and post-treatments, Journal of Manufacturing Processes 64 (2021) 161–187.

[14] C. Romero, F. Yang, L. Bolzoni, Fatigue and fracture properties of ti alloys from powder-based processes–a review, International Journal of Fatigue 117 (2018) 407–419.

[15] S. Leuders, T. Lieneke, S. Lammers, T. Tröster, T. Niendorf, On the fatigue properties of metals manufactured by selective laser melting—the role of ductility, Journal of Materials Research 29 (17) (2014) 1911–1919.

[16] A. Cutolo, C. Elangeswaran, C. de Formanoir, G. K. Muralidharan, B. Van Hooreweder, Effect of heat treatments on fatigue properties of ti–6al–4v and 316l produced by laser powder bed fusion in as-built surface condition, in: TMS 2019 148th Annual Meeting & Exhibition Supplemental Proceedings, Springer, 2019, pp. 395–405.

[17] S. Cecchel, S. Mohammad Javad Razavi, F. Mega, G. Cornacchia, A. Avanzini, D. Battini, F. Berto, Fatigue testing and end of life investigation of a topology optimized connecting rod fabricated via selective laser melting 107134doi:10.1016/j.ijfatigue.2022.107134.
URL https://www.sciencedirect.com/science/article/pii/S0142112322003905

[18] R. Molaei, A. Fatemi, N. Sanaei, J. Pegues, N. Shamsaei, S. Shao, P. Li, D. Warner, N. Phan, Fatigue of additive manufactured ti-6al-4v, part ii: The relationship between microstructure, material cyclic properties, and component performance, International Journal of Fatigue 132 (2020) 105363.

[19] P. Li, D. Warner, N. Phan, Predicting the fatigue performance of an additively manufactured ti-6al-4v component from witness coupon behavior, Additive manufacturing 35 (2020) 101230.

[20] C. Elangeswaran, A. Cutolo, S. Gallas, T. D. Dinh, N. Lammens, H. Erdelyi, M. Schulz, G. K. Muralidharan, L. Thijs, T. Craeghs, et al., Predicting fatigue life of metal lpbf components by combining a large fatigue database for different sample conditions with novel simulation strategies, Additive Manufacturing (2021) 102570.

[21] C. Elangeswaran, A. Cutolo, G. K. Muralidharan, C. de Formanoir, F. Berto, K. Vanmeensel, B. Van Hooreweder, Effect of post-treatments on the fatigue behaviour of 316l stainless steel manufactured by laser powder bed fusion, International Journal of Fatigue 123 (2019) 31–39.

[22] C. Elangeswaran, A. Cutolo, G. K. Muralidharan, K. Vanmeensel, B. Van Hooreweder, Microstructural analysis and fatigue crack initiation modelling of additively manufactured 316l after different heat treatments, Materials & Design 194 (2020) 108962.

[23] C. Elangeswaran, K. Gurung, R. Koch, A. Cutolo, B. Van Hooreweder, Post-treatment selection for tailored fatigue performance of 18ni300 maraging steel manufactured by laser powder bed fusion, Fatigue & Fracture of Engineering Materials & Structures 43 (10) (2020) 2359–2375.

[24] Tech specs | 3d systems.
URL https://www.3dsystems.com/materials/laserform-ti-gr-23/tech-specs

[25] A. Cutolo, C. Elangeswaran, B. Van Hooreweder, On the effect of the stress ratio on fatigue properties of ti-6al-4v produced by laser powder bed fusion, Material Design & Processing Communications 2022 (2022).

[26] T. Nicholas, Step loading for very high cycle fatigue, Fatigue & Fracture of Engineering Materials & Structures 25 (8-9) (2002) 861–869.

[27] R. S. Bellows, S. Muju, T. Nicholas, Validation of the step test method for generating haigh diagrams for ti–6al–4v, International Journal of Fatigue 21 (7) (1999) 687–697.

[28] A. Cutolo, C. Elangeswaran, G. K. Muralidharan, B. Hooreweder, On the fatigue notch sensitivity of Ti-6Al-4V specimens with $\alpha+\beta$ microstructure produced by laser powder bed fusion (2021).

[29] C. E. Rasmussen, C. K. I. Williams, Gaussian processes for machine learning (2006).

[30] D. Duvenaud, Automatic model construction with Gaussian processes, Ph.D. thesis, University of Cambridge (2014).

[31] H. Neuber, Theory of notch stresses: principles for exact stress calculation of strength with reference to structural forms and materials, AEC TR 4547 (1958).

[32] L. Susmel, D. Taylor, A novel formulation of the theory of critical distances to estimate lifetime of notched components in the medium-cycle fatigue regime 30 (7) 567–581, _eprint: https://onlinelibrary.wiley.com/doi/pdf/10.1111/j.1460-2695.2007.01122.x. doi:10.1111/j.1460-2695.2007.01122.x.
URL https://onlinelibrary.wiley.com/doi/abs/10.1111/j.1460-2695.2007.01122.x

Declaration of interests

☒ The authors declare that they have no known competing financial interests or personal relationships that could have appeared to influence the work reported in this paper.

☐ The authors declare the following financial interests/personal relationships which may be considered as potential competing interests: